Nanoscale residual stress depth profiling by Focused Ion Beam milling and eigenstrain analysis

A.M. Korsunsky [a,*], E. Salvati [a], A.G.J. Lunt [a,b], T. Sui [a,e], M.Z. Mughal [c], R. Daniel [d], J. Keckes [d], E. Bemporad [c], M. Sebastiani [c]

[a] University of Oxford, Department of Engineering Science, Parks Road, Oxford, UK
[b] CERN, Route de Meyrin, Geneva, Switzerland
[c] Roma Tre University, Engineering Department, via della Vasca Navale 79, 00146 Rome, Italy
[d] Montanuniversität Leoben, Leoben, Austria
[e] Department of Mechanical Engineering Sciences, University of Surrey, Guildford GU2 7XH, UK

HIGHLIGHTS

- The use of multiple micro-ring-core FIB-DIC analysis for residual stress profiling is proposed.
- Eigenstrain analysis is used to reconstruct residual stress variation at resolution of 50 nm.
- Results are validated against nanofocus synchrotron X-ray diffraction data.

GRAPHICAL ABSTRACT
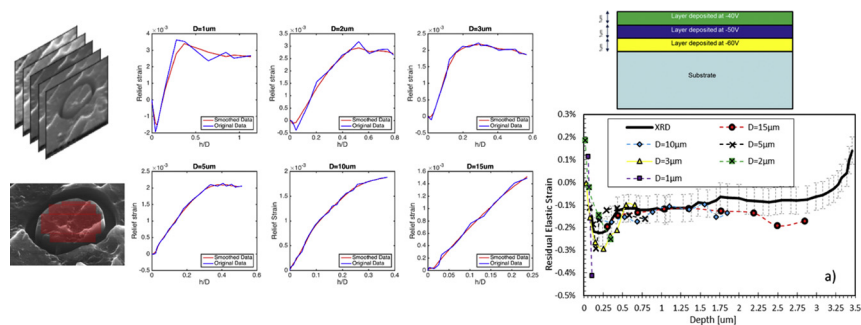
ARTICLE INFO

ABSTRACT

Residual stresses play a crucial role in determining material properties and behaviour, in terms of structural integrity under monotonic and cyclic loading, and for functional performance, in terms of capacitance, conductivity, band gap, and other characteristics. The methods for experimental residual stress analysis at the macro- and micro-scales are well established, but residual stress evaluation at the nanoscale faces major challenges, e.g. the need for sample sectioning to prepare thin lamellae, by its very nature introducing major modifications to the quantity being evaluated.

Residual stress analysis by micro-ring core Focused Ion Beam milling directly at sample surface offers lateral resolution better than 1 μm, and encodes information about residual stress depth variation. We report a new method for residual stress depth profiling at the resolution better than 50 nm by the application of a mathematically straightforward and robust approach based on the concept of eigenstrain. The results are validated by direct comparison with measurements by nano-focus synchrotron X-ray diffraction.

© 2018 Elsevier Ltd. All rights reserved.

1. Introduction

The presence of residual stress in mechanical components has a profound effect on their performance from the point of view of structural integrity and reliability [1,2]. Tensile residual stresses promote crack

* Corresponding author.
  E-mail address: alexander.korsunsky@eng.ox.ac.uk (A.M. Korsunsky).

nucleation and propagation from surface notches and internal flaws, while compressive residual stresses tend to improve the strength and fatigue resistance of components. However, stress is a scale-dependent concept that displays intricate interaction with the micro- and nano-structure of materials. By the early 1980's the classification of residual stresses became widely accepted into Type I, II and III stresses that can loosely be associated with the macro-, micro- and nano-scale [3–5]. The significance of Type II and III stresses became apparent in the context of the analysis of cracks, notches, surface machining, coating and thin film deposition, heat treatment, phase transformation, grain structure evolution, grain boundary fracture, creep damage and cavitation, corrosion and environmentally assisted cracking, etc. Several decades of modelling effort and careful reasoning pointed at the importance of incorporating the knowledge of micro-scale residual stresses into predictive modelling for reliable design. The principal difficulty in implementing this agenda lies primarily not in implementing numerical simulations that have been developing apace, but in the absence of reliable, universal, flexible and generic reference-free methods for the evaluation of residual stress across the scales, down to the smallest relevant structural dimensions of a few tens of nanometres.

Accurate evaluation of the residual stress is of crucial importance for rational design. For instance, the analysis of thin (multi)layers is of paramount importance for coated systems in which correct prediction of failure conditions must take into account the residual stress distribution through the film thickness. Several techniques are available for the experimental assessment of residual stress depth profile at different length scales. One of the most common non-destructive techniques is X-ray diffraction [6–9]. The recent developments in the generation of nano-focused X-ray beams have allowed probing the stress variation at the nanometre scale [10,11]. A related class of techniques is associated with spectroscopic methods, such as Fourier transform infrared spectroscopy (FTIR) [12] and Raman [13,14]. A further technique that is important to mention, not belonging to the X-ray family, is the well-established method used residual stress in films based on surface curvature analysis using the Stoney equation [15].

Another family of experimental techniques includes destructive methods that rely on material removal causing the modification of boundary conditions that leads to measurable changes in displacement or strain. Numerous variants have been developed for application at the macro- and down to micro- scale, e.g. the contour method. A subset of this family are techniques that are semi-destructive, in that they involve minimal modification of sample surface e.g. by 'blind' or through hole drilling [16–18], ring-core [19,20], cantilever deflection [21], slot cutting [22] slitting [23,24] and nanoindentation [25–27]. Material removal at the macroscopic scale can be performed by conventional tools (e.g. drilling, milling, electric discharge machining), and strain relief can be monitored by the application of strain gauge rosettes or using Digital Image Correlation (DIC) that allows full field displacement mapping and strain calculation. When the evaluation of residual stress is sought at the (sub) micron scale, the material removal process can no longer be conducted by conventional machining tools, and more refined means are required. Focused Ion Beam (FIB), coupled with Scanning Electron Microscope (SEM) allows the combination of material removal and displacement evaluation with the accuracy of the order of a few nanometres. The FIB-DIC micro-ring-core variant has become probably the most widespread technique for the evaluation of residual stress at the micro- to nano-scale, and has been shown to be capable of mapping Type II and III stresses [28,29,4,30], by incremental FIB milling of annular trenches and continuous image acquisition of the surface of the produced micro-pillar, with subsequent strain relief interpretation by DIC post-processing.

The structure of the present report is as follows. Section 2 introduces the materials and experimental techniques used in the study, including the samples and their fabrication, electron and ion microscopy procedures, and the basic interpretation procedures. Section 3 is devoted to the derivation and analysis of the novel approach to residual stress

depth profiling using eigenstrain-based analysis of multiple diameter micro-ring-core FIB-DIC data. The key relationships are presented, quantified, and incorporated in the interpretation procedure. Section 4 is devoted to the application of the procedure, the newly developed approach is applied to the evaluation of residual stress variation with depth for the samples chosen for this study. The capability of the method to achieve ~50 nm resolution is demonstrated. To the best of the authors' knowledge, there is no source in the literature that reports residual stress depth-profiling by a means that obviates the need for complex and destructive sample preparation procedures, such as TEM lamellae milling, or the fabrication of micron-thin samples for synchrotron nano-diffraction – the method that is used for cross-validation of the new technique in the present report.

2. Materials and methods

2.1. Materials

The sample was composed of a 375 μm-thick Si wafer which was coated with a nanocrystalline TiN multi-layer thin film. Reactive pulsed DC magnetron sputtering was performed using industrial-scale CemeCon CC800/9 MLT which was equipped with four unbalanced magnetrons and Ti targets (99.97% purity) of dimension $500 \times 88 \times 10$ mm^3. The films were deposited at 550 °C on double-sided polished Si (100) substrates (of size 20×7 mm^2). Before deposition the wafers were ultrasonically cleaned in acetone and ethanol for 10 min, and were then sputter-etched in an argon plasma discharge. During deposition the magnetrons were operated in constant power mode at 7 kW (corresponding to 600 V) per target at 50 kHz. During deposition, the asymmetric bipolar pulsed DC bias voltage U_b at the substrate holder was varied in three stages corresponding to the values of −60 V, −50 V and −40 V at 350 kHz and 1.0 μs reversal time, corresponding to the duty cycle (fraction of time during each period when voltage was applied) of 65%. By considering the information provided in the literature, the appropriate values of Young's modulus and the Poisson ratio for the coating film were chosen as 400 GPa and 0.25, respectively [31].

The films consisted of three sub-layers of equal thickness ~1 μm deposited under different conditions, and therefore expected to contain different residual stress states (Fig. 1). A constant flow of Ar and N$_2$ was used to obtain a nitrogen partial pressure of $P_{N2} = 0.25$ Pa and a total pressure $P_{tot} = 0.6$ Pa (corresponding to $P_{N2}/P_{Ar} = 0.4$). The base pressure in the deposition chamber was $\leq 4 \cdot 10^{-3}$ Pa. After 165 min of deposition, in which there were two complete cycles of substrate rotation, a uniform film thickness of 3.2 ± 0.1 μm was obtained across the entire wafer.

2.2. XRD measurements

Transmission X-ray diffraction was performed at the nano-focus extension of the ID13 beamline at the European Synchrotron Radiation Facility (ESRF), Grenoble, France. 100 μm-thick slices of the substrate and
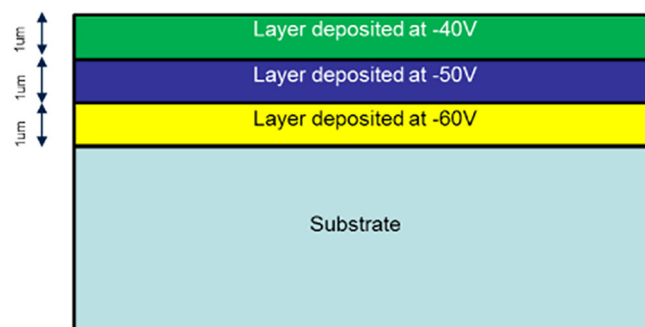

Fig. 1. Schematic representation of the coated sample structure.

thin film were prepared using a sectioning process, followed by careful polishing. The specimens were then mounted and the substrate-coating interface was aligned with the 14.9 keV monochromatic incident beam. The beam was focused to a size of 150×200 nm (V $\times$ H) and the sample was incrementally rastered in a direction perpendicular to coating surface at a step size of 100 nm. The 2D Debye-Scherrer ring patterns collected by the detector were interpreted using the software Fit2D which was used to extract equivalent 1D diffraction profiles from selected sectors. Gaussian peak fitting was then used to determine the variation of the (111) and/or (200) lattice parameters, in directions aligned with the sample preferred orientation. The strain components determined using XRD were then combined to evaluate the pre-existing residual stress distribution in the film using the procedure developed by Daniel et al. [32].

2.3. FIB-DIC measurements

In order to obtain the residual stress depth profile within the multi-layer coating, six separated FIB-DIC micro-ring-core experiments were carried out. The idea used in the present study was to employ ring-core features of different diameters, because prior modelling and experimental studies by the authors revealed that the depth of maximum sensitivity to the residual stress in the sample scaled proportionally to the core diameter, due to the geometric similarity. To take this principle further, the data obtained from different core diameter experiments can be combined to improve the resolution and statistical reliability of the results. Consequently, the six different core diameters used in the present study were $D_1 = 1$ μm, $D_2 = 2$ μm, $D_3 = 3$ μm, $D_4 = 5$ μm, $D_5 = 10$ μm and $D_6 = 15$ μm, respectively. This ensured good sensitivity and stress profile evaluation at different depths. The smaller micro-pillar diameters provided sensitivity to the residual stress in the vicinity of sample surface, while larger ring-core diameters provided improved insight into residual stresses at deeper positions within the sample. The information obtained at different depth ranges was combined to reconstruct the overall residual stress profile.

An example of FIB-DIC ring-core image obtained during milling is given in Fig. 2, together with the superimposed DIC grid used for

Fig. 2. SEM image taken during FIB-DIC milling process. The red markers indicate the DIC analysis grid covering 80% of the micro-pillar diameter (see Methods section). (For interpretation of the references to colour in this figure legend, the reader is referred to the web version of this article.)

displacement tracking. The grid used in this case study corresponds to the 80% of reduction factor φ.

A Matlab based DIC routine [33] was used for automatic evaluation of the average strain change at each milling step with respect to the original image of material surface prior to milling. The evolution of the strain relief was extracted so that the strain relief profiles could be plotted. The raw data obtained from DIC analysis was post-processed by applying a Savitzky–Golay filter [34] that performs moving average smoothing and can be applied to non-equispaced data. A linear function with the span of 3 experimental points was used in the present case. Although, higher order polynomial functions or larger span range could also be used, the above choice introduces minimal changes to the raw data, and was preferred.

3. Derivation and analysis

3.1. Eigenstrain depth profiling approach

Residual stress evaluation based on strain relief requires the reconstruction of the residual stress profile by inverse analysis. The state-of-the-art approach is the integral method by Schajer et al. [35–37] based on the mathematical relationship between the pre-existing residual stress σ at depth (denoted z) and the observed strain relief as a function of the drilling depth h:

$$e(h) = \frac{1}{E} \int_o^h F(h,z)\, \sigma(z)\, \mathrm{d}(z) \tag{1}$$

Here E is the material's Young's modulus. The kernel function $F(h,z)$ in the above equation necessarily depends on two parameters, since the influence of residual stress at all shallower depths $z < h$ must be accounted for. The solution of the above equation involves its discretisation to produce a triangular matrix containing the so-called calibration coefficients calculated by FEM, and inversion of this discrete form. The method has become well established and provides a reliable approach to residual stress depth profiling, but the determination of calibration coefficients is a time-consuming and sample-specific exercise, particularly when high depth resolution is sought by using small increments and large number of milling steps.

The formulation we propose in the present manuscript relies on the choice of eigenstrain, or misfit strain, as the main unknown quantity that needs to be determined. Eigenstrain has been the subject of extensive research work in the past few decades [38–42], since the introduction of the term by T. Mura [43]. It has been demonstrated that unlike residual stress that is extrinsic, i.e. sensitive to the changes in the sample geometry due to even most careful material removal, eigenstrain is an intrinsic parameter that is inherent to the material analysed and represents the material 'memory' of the deformation and processing history. Provided no introduction of new eigenstrain (inelastic deformation) occurs during material removal, the eigenstrain remains unchanged throughout the drilling process. In contrast with the classical integral method for residual stress depth profiling, eigenstrain analysis of each incremental milling step can be conducted separately, leading to complete decoupling between increments. This opens the possibility of formulating the relationship between eigenstrain and strain relief increment in terms of a simple multiplicative factor, as detailed below.

The strain relief at depth h in terms of eigenstrain at depth z is given by:

$$e(h/D) = \int_o^{\frac{h}{D}} F\left(\frac{z}{D}\right) \epsilon^*(z)\, \mathrm{d}\left(\frac{z}{D}\right) \tag{2}$$

Here h/D is the normalised milling depth, z/D is the normalised depth at which eigenstrain is being determined, and $\epsilon^*(z)$ is the a priori unknown eigenstrain distribution. $F\left(\frac{z}{D}\right)$ is the *single variable* master
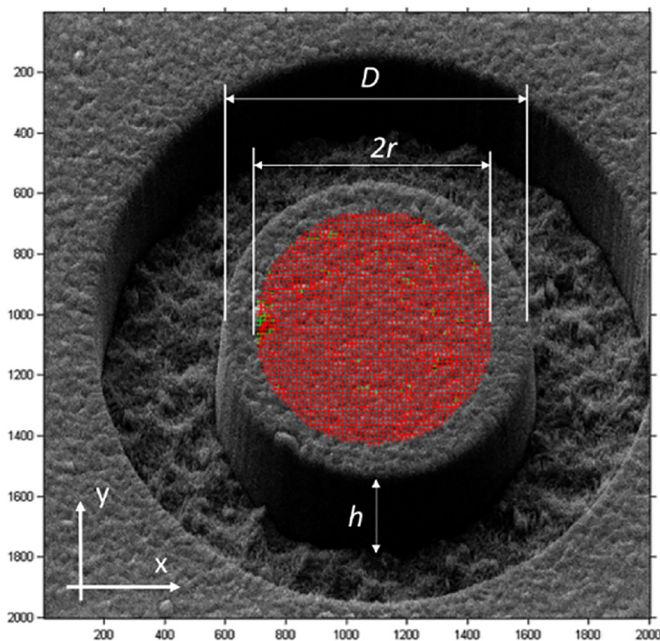
influence function that describes the incremental contribution to the surface strain relief from eigenstrain $\epsilon^*(z)$.

The mathematical basis of the formulation is the principle of superposition due to the linearity of the eigenstrain problem of elasticity. It has been demonstrated [38] that the direct problem of eigenstrain corresponds to the classical problem of elasticity that is perturbed by the inhomogeneous right hand side of Saint Venant's equations of strain compatibility. The assumption of eigenstrain invariance remains valid, provided any additional inelastic deformation that may arise in the course of ring-core milling is negligible. This assumption may be violated due to ion beam damage, in case of FIB milling, although our studies have shown that this effect is typically limited to a thin layer not exceeding ~30 nm at the periphery of the micro-pillar, and therefore can be neglected for ring-core sizes in excess of ~1 μm [29,44,45,42,46]. Plastic deformation may also arise due to the stress concentration at the bottom of the milling trench. This effect may be particularly significant at the early stages of milling, suggesting that the data obtained at shallow normalised milling depths should be treated with caution, as detailed below.

Due to the invariance of eigenstrain, the influence function $F(\frac{z}{D})$ depends on the single variable z/D. This notable feature of the above formulation means that the solution for the unknown function $\epsilon^*(z)$ can be obtained using a straightforward approach. By differentiating Eq. (2) with respect to the variable h/D, the following non-integral relationship is obtained:

$$\frac{de(h/D)}{d(h/D)} = \left[F\left(\frac{z}{d}\right)\epsilon^*(z) \right]_{z=h} = F\left(\frac{h}{D}\right)\epsilon^*(h) \tag{3}$$

Therefore, the eigenstrain distribution is found by division:

$$\epsilon^*(h) = \frac{de(h/D)}{d(h/D)} / F\left(\frac{h}{D}\right) \tag{4}$$

In terms of the numerical implementation, the most straightforward way of solving the above equation is by considering the discrete formulation:

$$\epsilon^*(h_i) = \frac{\Delta e(h_i/D)}{\Delta h_i/D} / F\left(\frac{h_i}{D}\right) \tag{5}$$

The eigenstrain at depth h_i can be computed by evaluating the strain relief difference between e_i at milling depth h_i and its previous value e_{i-1} at the previous depth h_{i-1}:

$$\epsilon^*(h_i) = \frac{e(h_i/D) - e(h_{i-1}/D)}{(h_i - h_{i-1})/D} / F\left(\frac{h_i}{D}\right) \tag{6}$$

A further correction can be introduced in the numerical algorithm by associating the eigenstrain value calculated with the mid-depth position between depths h_i and h_{i-1}:

$$h_i^* = \frac{h_i + h_{i-1}}{2} \tag{7}$$

Eigenstrain at depth h_i^* is therefore written as:

$$\epsilon^*(h_i^*) = \frac{e(h_i/D) - e(h_{i-1}/D)}{(h_i - h_{i-1})/D} / F\left(\frac{h_i^*}{D}\right) \tag{8}$$

For the purpose of calibration it is necessary to perform numerical calculation for a reference case to obtain the values of the master influence function depending on its normalised depth argument, $F(h_i/D)$. For this it suffices to consider the case of material being subjected to uniform negative eigenstrain field of strength unity, giving rise to the cumulative strain relief function that is denoted $f(h/D)$. Eq. (2) for this

case is written as follows:

$$e(h/D)_{\epsilon^*=-1} = f(h/D) = \int_0^{\frac{h}{D}} F\left(\frac{z}{D}\right) d\left(\frac{z}{D}\right) \tag{9}$$

By differentiating this equation, the incremental master influence function is evaluated as follows:

$$F\left(\frac{h}{D}\right) = \frac{d[e(h/D)]_{\epsilon^*=-1}}{d\left(\frac{h}{D}\right)} = \frac{d[f(h/D)]}{d\left(\frac{h}{D}\right)} \tag{10}$$

In practice, the (incremental) master influence function $F(h/D)$ can be extracted by differentiating the strain relief curve $f(h/D)$ generated from the simulation of FIB-DIC micro-ring-core milling of a material containing uniform negative eigenstrain of strength unity.

Once the abstraction of eigenstrain component is accomplished, residual stress is calculated by means of applying the appropriate version of the generalised Hooke's law. Micro-ring-core milling to the normalised depth $(h/D) \geq 1$ causes complete relief of residual elastic strain ε. Provided the substrate is sufficiently thick and that the ratio is small between the characteristic length (ring-core diameter) D and the component local curvature ρ, the conversion between eigenstrain and the residual elastic strain amounts only to changing sign:

$$\varepsilon = -\epsilon^* \tag{11}$$

To define the complete in-plane elastic strain tensor, the knowledge of residual strain for at least three different directions is required. In the more general case, the knowledge of strain along n multiple directions $(n > 3)$ can be used to formulate a minimisation problem that seeks the principal stress components and their associated orientations that enforce the strain transformation equations in the least-squares sense. Once the three components of strain or the principal strains are known, the problem is reduced to the simple solution of the rosette strain gauge equations, earlier shown by Lunt et al. [47]. By introducing the assumption that out-of-plane residual stress components are close to zero in the gauge volume, the complete stress tensor can be evaluated by means of the appropriate form of Hooke's law:

$$\begin{bmatrix} \sigma_1 \\ \sigma_2 \\ \sigma_{12} \end{bmatrix} = \frac{E}{(1-\nu^2)} \begin{bmatrix} 1 & \nu & 0 \\ \nu & 1 & 0 \\ 0 & 0 & \frac{1-\nu}{2} \end{bmatrix} \begin{bmatrix} \varepsilon_1 \\ \varepsilon_2 \\ 2\varepsilon_{12} \end{bmatrix} \tag{12}$$

For the particular case where the probed material shows highly elastic anisotropic behaviour, the assessment of residual stress can be computed by following the calculation framework proposed by Salvati [48]. The same paper provides quantitative evaluation of uncertainty in stress calculation in the case of unknown underlying material crystal orientation, a common situation when dealing with residual stress measurement at the micron-scale in polycrystalline materials.

Following, the procedure for the determination of the master influence function for the FIB-DIC micro ring-core method using FEA is shown. This function is generic and can be used for the microscopic version of the ring-core method, this is possible due to the non-dimensional formulation of the problem implemented.

Complete strain relief is achieved at the top surface of the ring-core milled micro-pillar once the milling depth equals its diameter [49]. Therefore, a material removal process was simulated up to the point where the milling depth h reaching the ring-core diameter D, i.e. for $h/D \leq 1$ (Fig. 3).

Fig. 4 illustrates that rapid change in the strain relief occurs at small milling depths. Hence, the milling step was refined for the shallowest region of material to ensure that the strain relief curve could be captured accurately. To reduce the computational effort, axial symmetry was imposed on the boundary conditions in the plane of the sample
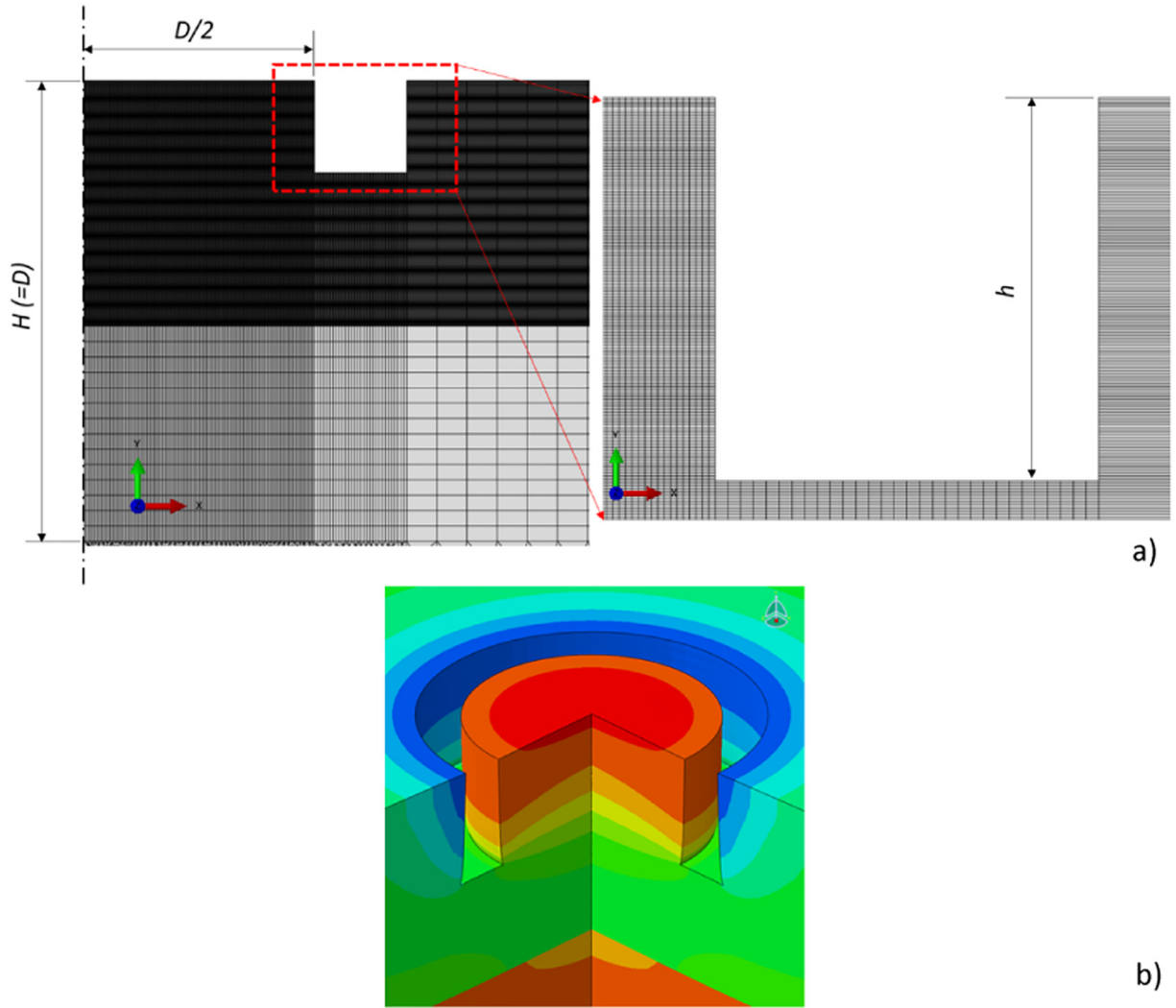
Fig. 3. (a) FE mesh used in the simulation and close-up of the vicinity of the free surface showing mesh refinement. (b) Elastic strain contour plot at the normalised milling depth ratio $h/D = 0.5$.

surface in terms of the boundary conditions. An example of the elastic strain contour at the normalised milling step of $h/D = 0.5$ is illustrated in Fig. 3(b).

In accordance with the common implementation of the FIB-DIC micro-ring-core method, we average the strain relief in the radial direction. The plot of the strain relief curve as a function of the normalised
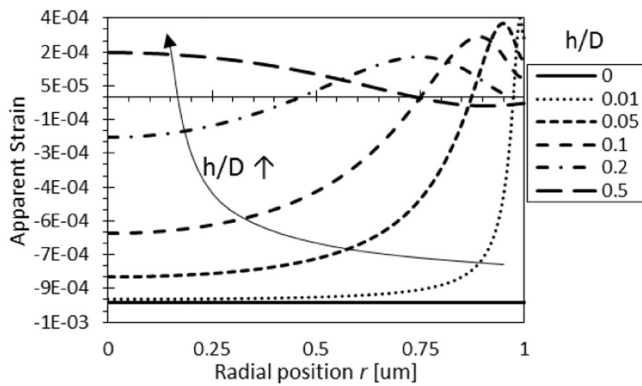
Fig. 4. Elastic strain evolution with the normalised milling depth h/D. Each curve represents the strain distribution over the pillar's surface as function of normalised radial position **r**.

milling depth is shown in Fig. 5 [47]. In practice, the average value of strain perceived by DIC is typically calculated not over the entire ring-core micro-pillar surface, but within a more confined area that we refer to as the *effective area*. The reason for this feature of implementation is that the periphery of the ring-core micro-pillar is typically affected by FIB milling or drilling artefacts that prevent reliable DIC interpretation. For the sake of convenience, we identify the reduced area with respect to the nominal area covering the complete ring-core micro-pillar surface by a reduction factor φ of the ring-core radius, $r = \varphi R = \varphi D/2$. The *effective area* is given by

$$A_e = \pi(\varphi R)^2 \tag{13}$$

We perform the calculation of average strain relief for three values of parameter $\varphi = 1$, 0.8 and 0.6. The strain relief evolution as a function of the normalised milling depth h/D for all three cases could be fitted to the precision better than 1% using a combination of quadratic and exponential functions using the form:

$$f\left(\frac{h}{D}\right) = 1 - \exp^{-\alpha\left(\frac{h}{D}\right)}\left[1 + \beta\left(\frac{h}{D}\right) - \gamma\left(\frac{h}{D}\right)^2\right] \tag{14}$$

The values of three parameters obtained by least-squares fitting are summarised in Table 1 below.
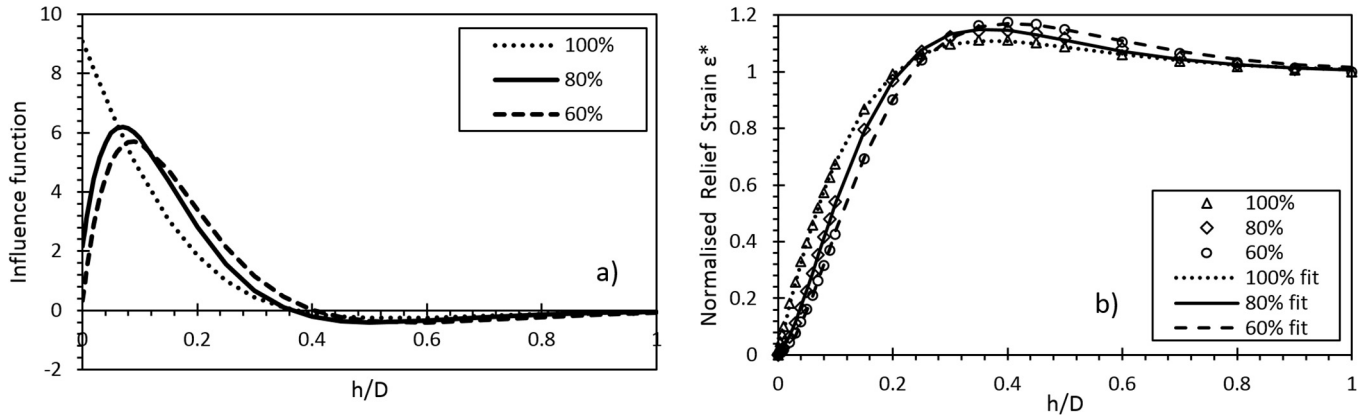
Fig. 5. (a) FE results for the strain relief curves $f(h/D)$ (markers) and closed form fits (continuous curves). (b) Master influence functions $F(h/D)$ obtained by differentiation of strain relief curves.

According to Eq. (10), the (incremental) master influence function can now be found by analytical differentiation of the relief curve with respect to the normalised depth variable, as follows:

$$F\left(\frac{h}{D}\right) = \frac{df\left(\frac{h}{D}\right)}{d\left(\frac{h}{D}\right)}$$

$$= \exp^{-\alpha\left(\frac{h}{D}\right)}\left[\alpha - \beta + \alpha\beta\left(\frac{h}{D}\right) + 2\gamma\left(\frac{h}{D}\right) - \alpha\gamma\left(\frac{h}{D}\right)^2\right] \quad (15)$$

In Fig. 5, along with the strain relief curves for different reduction factors of the effective averaging area (Fig. 5(a)), the differentiations are also shown in Fig. 5(b).

The results presented above reveal important information regarding the method's sensitivity. For the range of normalised depths $h/D = 0.015 \div 0.2$, high values of $F(h/D)$ are obtained (Fig. 5(b)). Therefore, the method possesses greatest sensitivity to eigenstrains at the depth $0.015D < h < 0.2D$. At milling depths below $0.015D$, the strain relief may be affected by the precise details of the milling geometry, such as the width of the annular milling trench and its taper angle, as well as the stress concentration at the bottom of the trench. At depths exceeding $0.2D$ the sensitivity of strain relief at the micro-pillar surface drops below the value of 2, and ultimately becomes negative. This introduces ambiguity into the interpretation. This situation can be avoided by deploying ring-cores of larger diameter, thus shifting the method's sensitivity range to larger absolute depths.

The calibration of this function and the procedure for the inversion are described in the Section 2 of this paper. Fig. 5 illustrates the calibration of the strain relief curves based on strain averaging across different fractions of the entire pillar area.

The principal features of the described procedure are:

1) The use of micro-ring-core milling geometry which causes progressive strain relief that generally corresponds to the progression of the stress state within the gauge volume towards the origin in the stress space, minimising the likelihood of plastic flow.

2) The obviation of the necessity of matrix inversion that forms the central element of the previous methods, and its replacement with direct calculation of the eigenstrain value at given depth by strain relief increment division by the factor related to the derivative of the influence function.

3) The reduction of dependence on material elastic properties due to the underlying relationships being cast entirely in terms of strains.

4) The reduction of required analysis for the determination of the master influence function of a single variable (depth) that encapsulates all dependence of (incremental) strain relief on the micro-ring-core milling gauge volume geometry.

5) The introduction of convenient, high precision, closed form expressions for the influence function that facilitate subsequent manipulation and analysis.

6) The identification of the method's sensitivity as a function of the relative milling depth that allows the micro-ring-core feature diameter to be tailored to the required depth of residual stress determination.

The non-integral method of residual strain and stress profiling proposed in the present paper possesses several important advantages and overcomes some of the limitations of the current state-of-the-art, in that it removes the strong dependence on material's elastic properties, obviates the need for matrix calculation, equips the users with efficient closed form solution, provides a firm rational basis for combined use of multiple ring-core diameters, and is validated by the excellent agreement with independent measurement using synchrotron XRD strain analysis. The single master influence function can be used to invert the strain relief profile data to abstract the eigenstrain depth profile, and to evaluate the underlying residual stress within the material. Provided the substrate is sufficiently thick and that the ratio is small between the characteristic length (ring-core diameter) D and the component local curvature ρ, the conversion between eigenstrain and the residual elastic strain amounts only to changing sign. Residual stress can then be calculated using Hooke's law in appropriate form.

The application of the proposed method can find extensive application in the analysis multi-layered films. In view of the great importance of residual stress depth profiling in this class of engineering systems, some remarks on the applicability of the present method to this problem are presented here.

The functionality of multi-layered coatings is established by exploiting the difference in the mechanical, chemical, magnetic, and other properties of the individual layers. For the purposes of residual stress analysis it is particularly important to investigate the influence of elastic properties contrast. FEM simulations of the milling process were run for a bi-layer system with the interface lying at the normalised depth $h/D = 0.015$, where D is the total thickness of the coating lying on a semi-infinite substrate. Three simulations were performed by

Table 1
Parameters of the closed form quadratic-exponential strain relief function $f(\frac{h}{D})$.

Parameter	Reduction factor φ		
	1 (100%)	0.8 (80%)	0.6 (60%)
α	7.575	8.813	7.944
β	−1.512	6.647	7.618
γ	16.452	53.852	50.940

imposing different elastic moduli ratios of the two layers, $E'/E = 1$, 2 and 4, where E' and E are Young's moduli of the bottom and top layers, respectively. It was assumed that uniform equi-biaxial eigenstrain distribution (and hence residual stress) was present within the coating. Strain relief was evaluated using 80% coverage ($\varphi = 0.8$).

The outcome of the FEM simulations was processed following the procedure described. The results are shown in Fig. 6.

From the plots shown in Fig. 6 it is clear that the response of the coated system to material removal during FIB milling depends on the elastic property contrast between the film and the substrate. This becomes particularly apparent by considering the influence functions. As already discussed, maximum sensitivity is achieved when the ring core diameters are chosen to be in the range $h/D = 0.015 \div 0.2$. In this region, even for the case of four-fold mismatch in the elastic modulus, the influence function values change by no more than ~20%. This indicates that the present method of reconstruction is robust, and can be used for residual stress estimation even in the absence of precise knowledge of the elastic properties of the coating.

4. Application

FIB-DIC measurements were conducted using a range of ring-core diameters from 1 μm to 15 μm (six different diameters) to ensure high sensitivity through the range of depths examined.

In order to validate the proposed eigenstrain depth profiling method and assess its accuracy, in this section we present a comparison of the results against the measurements obtained by nano-focus synchrotron X-ray diffraction. Fig. 2 provides an illustration of the sample surface at an intermediate stage of FIB-DIC analysis.

With reference to Fig. 5(b) and the accompanying influence function sensitivity analysis, the range of h/D was chosen to correspond to $0.015 < h/D < 0.2$ for each ring-core diameter data set. Ring-core milling features with smaller diameter contributed the data for residual strain in the vicinity of free sample surface, while ring-core features of larger diameter allowed residual elastic strain evaluation in deeper subsurface layers.

The reconstruction applied to multi-scale FIB-DIC micro-ring-core method led to the results that were validated against the independent nano-focus synchrotron XRD measurement. The combination of six different ring-core diameters allowed accurate residual elastic strain reconstruction to be carried out to the full layer depth of 3 μm. Fig. 7 illustrates the raw strain relief curves obtained by DIC analysis for all ring-core diameters, along with the profiles following smoothing filter processing.

The ultimate goal of the present case study was the evaluation of residual stress (residual strain) depth profile. Fig. 8 illustrates that the residual elastic strain evaluation obtained from ring-core features of different diameter was consistent. For the purposes of final comparison and validation against nano-focus SXRD data, obtained in the form of elastic lattice strains, a single profile curve was obtained. This was performed by linear data interpolation for each ring-core diameter, followed by averaging. The result is reported in Fig. 8 together with the residual elastic strain obtained from SXRD measurements. The error bars correspond to the 95% confidence intervals arising purely from the averaging process. Although the error estimation in the context of the micro-ring-core residual stress evaluation method is well-advanced [50], it represents a separate issue that needs to be addressed in the context of error propagation through the entire analysis, and it will be addressed separately.

By averaging the several ring-core diameters residual elastic strain profiles, a single depth profile could be obtained as depicted in Fig. 9 (a). An excellent agreement between the evaluated residual strain profiles. At depths in excess of 0.1 μm and <2.25 μm the residual strain values assessed by FIB-DIC lie within the error bars of SXRD measurement. As well as the residual elastic strain profiles, the residual stress can also be evaluated using the appropriate calculation based on Hooke's law, assuming equibiaxial stress state. The results are shown in Fig. 9(b). Remarkably, FIB-DIC provided data at the step resolution better than 50 nm, including in the very near-surface regions where SXRD data is absent due to the limitation of experimental setup. The ability to resolve the very near-surface residual stress profiles at nanometre resolution is crucial for the analysis of a wide range of systems of great significance for surface science, tribology, etc. For the depths > 2.25 μm some disagreement between FIB-DIC and SXRD results is observed that is likely to be associated with the lack of information from multiple smaller ring-core diameter measurements: in this range the residual elastic strain profile was obtained solely based on the interpretation of the depth profile obtained from 15 μm diameter ring-core dataset.

5. Discussion

The results presented in Section 4 demonstrate that the approach based on eigenstrain analysis of multiple micro-ring-core FIB-DIC data allows faithful reconstruction of near-surface residual stresses at depth up to ~3 μm, at the resolution as low as 50 nm or better. In Fig. 9 the three distinct layers deposited at different bias values are indicated using different colour shading. There is evidence of correlation between the deposition conditions and the resulting residual stress, although the intra-layer variation is also evident. The results demonstrate the remarkable ability of the new method to resolve very short range residual stress profiles.

The new approach opens unprecedented possibilities for short range analysis of sub-surface residual stresses in coatings and treated surfaces.
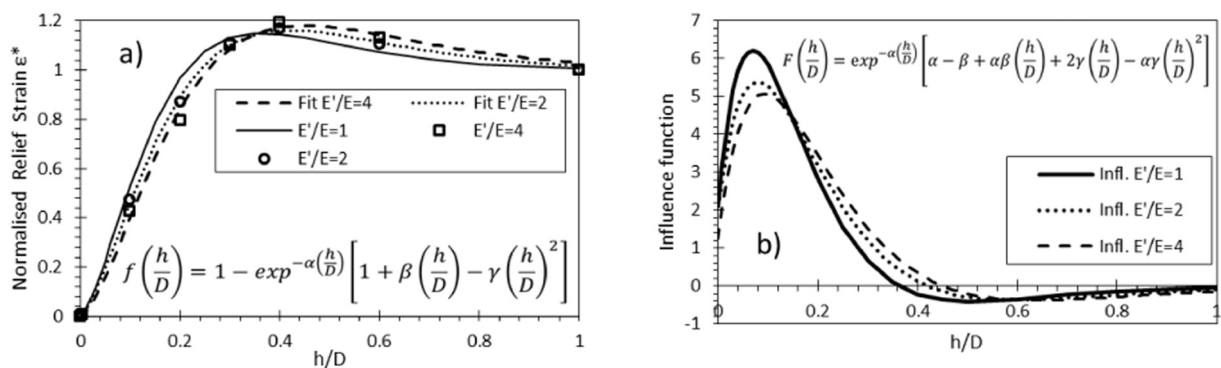

Fig. 6. FE results at different elastic properties ratios between the two layers. (a) FE results for the strain relief curves $f(h/D)$ (markers) and closed form fits (continuous curves). (b) Master influence functions $F(h/D)$ obtained by differentiation of strain relief curves.
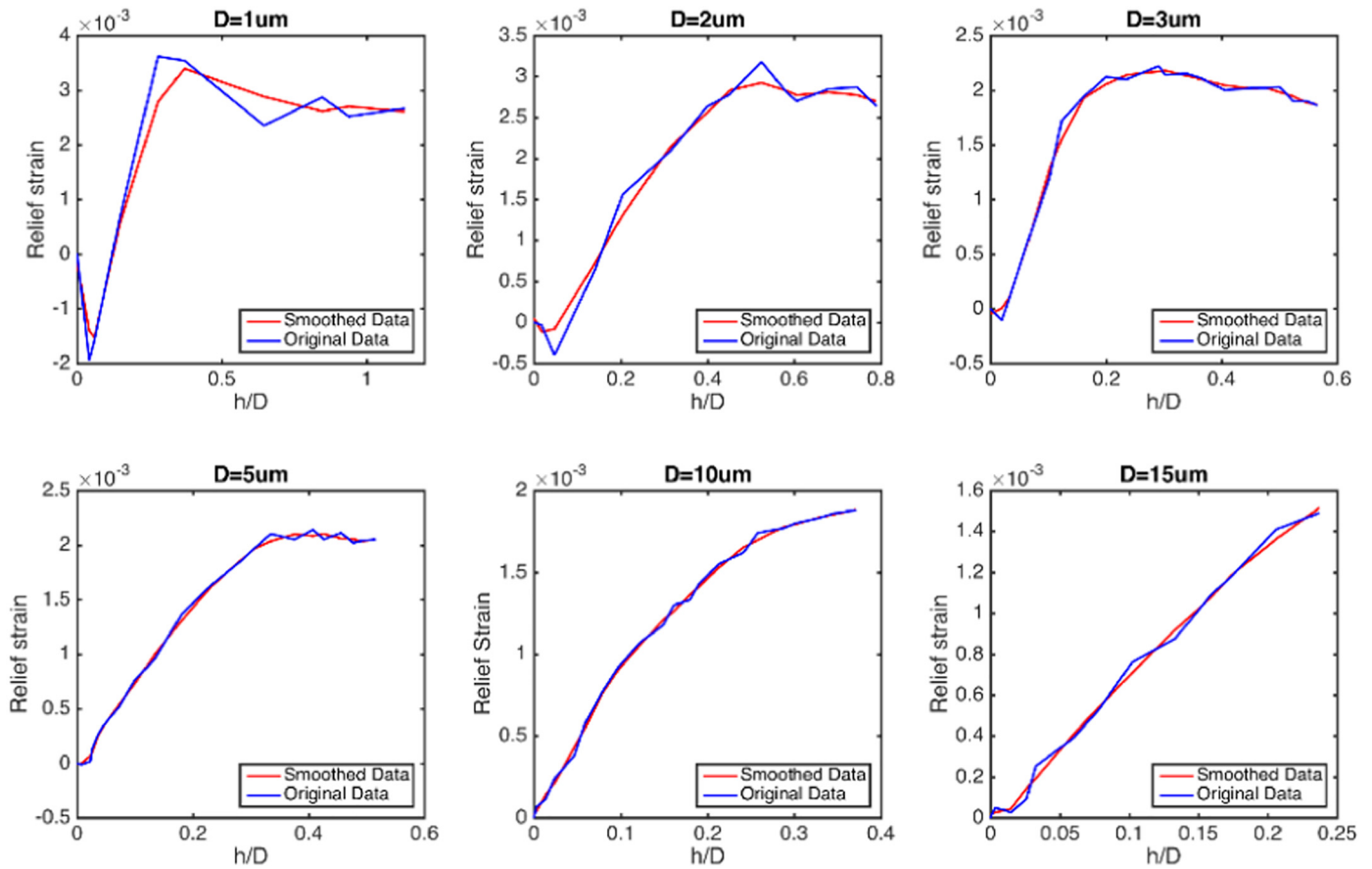
Fig. 7. Strain relief curves from DIC analysis of different pillar diameters, along with the profiles obtained after smoothing filter processing.

6. Conclusions

The non-integral method of residual strain and stress profiling proposed in the present paper overcomes many limitations of the current state-of-the-art and possesses several important advantages. It obviates the need for matrix calculation, equipping the user with efficient closed form solution. The approach has far-reaching implications, and can be used for macroscopic residual stress analysis using ring-core drilling, as well as for conventional blind hole drilling, by evaluating the appropriate influence functions. The approach provides a firm rational basis for the combined use of multiple ring-core diameters, resulting in close agreement with independent measurements by synchrotron XRD strain analysis. Furthermore, the dependence of the influence function on the elastic property mismatch within multi-layer coatings is found to be weak (see Section 3). The master influence function can be used to invert the strain relief profile data to abstract the eigenstrain depth profile, and to evaluate the underlying residual stress within the material. Provided the substrate is sufficiently thick and that the ratio is small between the characteristic length (ring-core diameter) D and the component local curvature ρ, direct conversion between eigenstrain and the residual elastic strain is obtained through simple change of sign, although more complex situations can also be considered using inverse eigenstrain. Residual stresses are calculated using the appropriate form of Hooke's law.
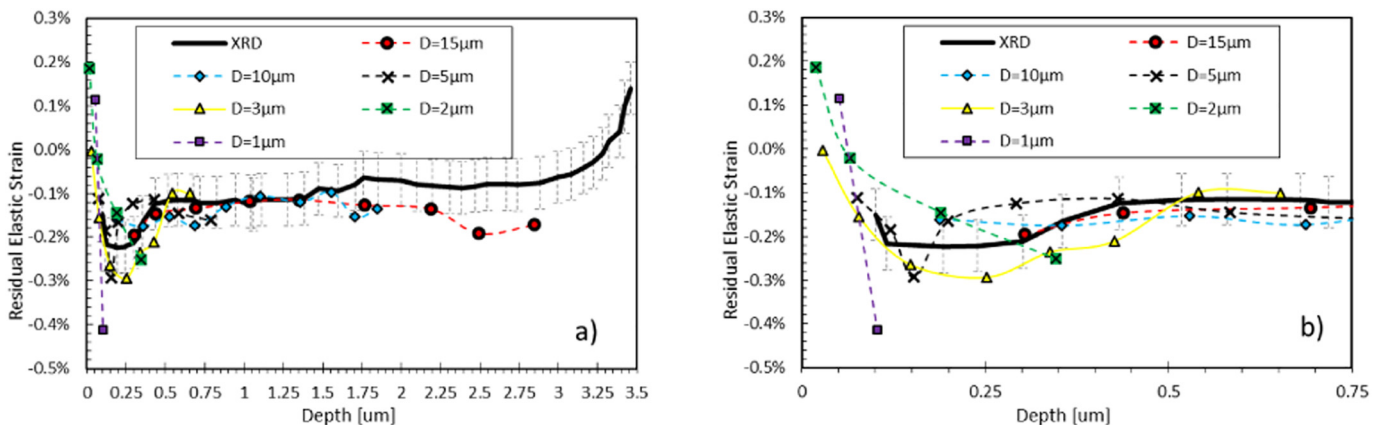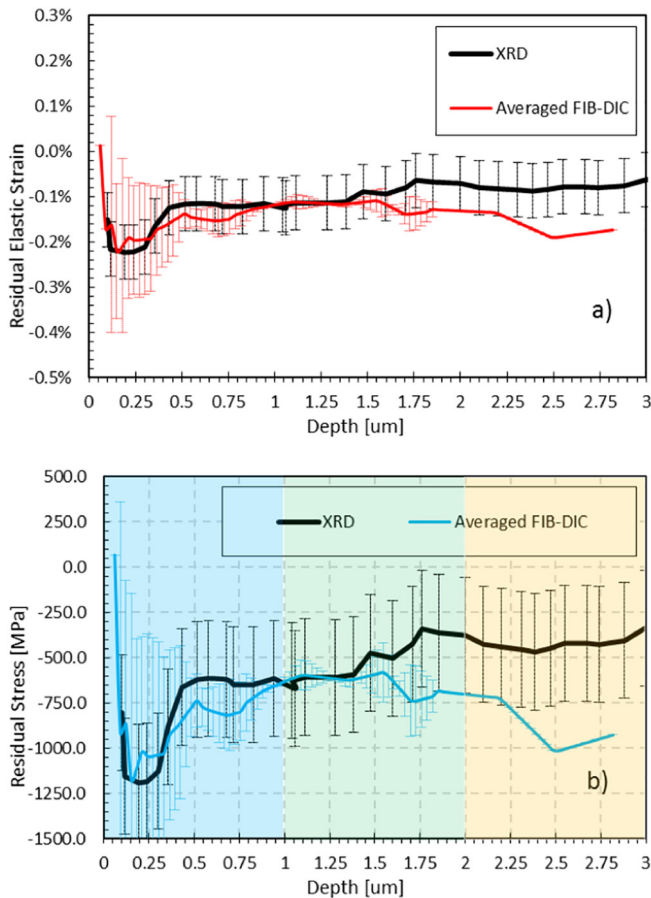

Fig. 8. (a) The residual strain profiles obtained by multi-scale FIB-DIC analysis. For each ring-core diameter the results were extracted for the milling depth range $0.015 < h/D < 0.2$, in accordance with the influence function sensitivity analysis (Fig. 6(b)). (b) Close up plot in the shallowest region.

Fig. 9. Results comparison for FIB-DIC vs XRD. The overall FIB-DIC profile was obtained by linear interpolation and averaging of the results shown in Fig. 8 for different ring-core feature diameters. a) Residual elastic strain and b) residual stress computed based on the assumption of equibiaxial stress state.

Acknowledgements

Data availability

Additional data can be accessed via ORA (http://ora.ouls.ox.ac.uk). The raw data used in the analysis containing the FIB-DIC strain relief obtained from multiple micro-ring-core millings has been made freely available at Mendeley Data: doi:10.17632/vb78jgkw4z.1

Request for any material samples or specimens described in this manuscript should be directed to the corresponding author.

References

[1] M.N. James, Residual stress influences on structural reliability, Eng. Fail. Anal. 18 (8) (2011) 1909–1920.
[2] P. Iurea, C. Carausu, Considerations concerning the causes and effects of the occurrence of residual stresses in metallic materials: a review, Appl. Mech. Mater. 659 (2014) 91–100.
[3] Viktor Hauk, Structural and Residual Stress Analysis by Nondestructive Methods, Elsevier Science B.V., Amsterdam, 1997 iii.
[4] E. Salvati, A.M. Korsunsky, An analysis of macro- and micro-scale residual stresses of type I, II and III using FIB-DIC micro-ring-core milling and crystal plasticity FE modelling, Int. J. Plast. 98 (2017) 123–138.
[5] L. Pintschovius, V. Jung, E. Macherauch, O. Vöhringer, Residual stress measurements by means of neutron diffraction, Mater. Sci. Eng. 61 (1) (1983) 43–50.
[6] E. Salvati, T. Sui, H. Zhang, A.J.G. Lunt, K.S. Fong, X. Song, A.M. Korsunsky, Elucidating the mechanism of fatigue crack acceleration following the occurrence of an underload, Adv. Eng. Mater. 18 (12) (2016) 2076–2087.
[7] J. Holmberg, A. Steuwer, A. Stormvinter, H. Kristoffersen, M. Haakanen, J. Berglund, Residual stress state in an induction hardened steel bar determined by synchrotron- and neutron diffraction compared to results from Lab-XRD, Mater. Sci. Eng. A 667 (2016) 199–207.
[8] S. Dufrenoy, T. Chauveau, R. Brenner, C. Fontugne, B. Bacroix, Modeling methodology for stress determination by XRD in polycrystalline materials, Adv. Mater. Res. 996 (2014) 106–111.
[9] V.M. Puzikov, V.F. Tkachenko, V.A. Tsurikov, XRD method for the determination of internal stresses in KDP crystals and their relationship to the anomalous biaxiality, Funct. Mater. 22 (3) (2015) 402–407.
[10] J. Todt, H. Hammer, B. Sartory, M. Burghammer, J. Kraft, R. Daniel, J. Keckes, S. Defregger, X-ray nanodiffraction analysis of stress oscillations in a w thin film on through-silicon via, J. Appl. Crystallogr. 49 (2016) 182–187.
[11] M. Stefenelli, R. Daniel, W. Ecker, D. Kiener, J. Todt, A. Zeilinger, C. Mitterer, M. Burghammer, J. Keckes, X-ray nanodiffraction reveals stress distribution across an indented multilayered CrN-Cr thin film, Acta Mater. 85 (2015) 24–31.
[12] P.J. Lezzi, M. Tomozawa, R.W. Hepburn, Confirmation of thin surface residual compressive stress in silica glass fiber by FTIR reflection spectroscopy, J. Non-Cryst. Solids 390 (2014) 13–18.
[13] W. Zhu, E. Marin, N. Sugano, G. Pezzotti, Tensor-resolved Raman spectroscopic analysis of wear-induced residual stress fields in long-term alumina hip-joint retrievals, J. Mech. Behav. Biomed. Mater. 66 (2017) 201–210.
[14] A. Bharatish, H.N. Narasimha Murthy, G. Aditya, B. Anand, B.S. Satyanarayana, M. Krishna, Evaluation of thermal residual stresses in laser drilled alumina ceramics using Micro-Raman spectroscopy and COMSOL Multiphysics, Opt. Laser Technol. 70 (2015) 76–84.
[15] G.C.A.M. Janssen, M.M. Abdalla, F. van Keulen, B.R. Pujada, B. van Venrooy, Celebrating the 100th anniversary of the Stoney equation for film stress: developments from polycrystalline steel strips to single crystal silicon wafers, Thin Solid Films 517 (6) (2009) 1858–1867.
[16] T. Valente, C. Bartuli, M. Sebastiani, A. Loreto, Implementation and development of the incremental hole drilling method for the measurement of residual stress in thermal spray coatings, J. Therm. Spray Technol. 14 (4) (2005) 462–470.
[17] S. Schuster, M. Steinzig, J. Gibmeier, Incremental hole drilling for residual stress analysis of thin walled components with regard to plasticity effects, Exp. Mech. 57 (9) (2017) 1457–1467.
[18] J.P. Nobre, M. Kornmeier, B. Scholtes, Plasticity effects in the hole-drilling residual stress measurement in peened surfaces, Exp. Mech. 58 (2) (2017) 369–380.
[19] M. Sebastiani, F. Massimi, G. Merlati, E. Bemporad, Residual micro-stress distributions in heat-pressed ceramic on zirconia and porcelain-fused to metal systems: analysis by FIB-DIC ring-core method and correlation with fracture toughness, Dent. Mater. 31 (11) (2015) 1396–1405.
[20] A. Ajovalasit, G. Petrucci, B. Zuccarello, Determination of nonuniform residual stresses using the ring-core method, J. Eng. Mater. Technol. ASME 118 (2) (1996) 224–228.
[21] W.A. Sasangka, C.L. Gan, D. Lai, C.S. Tan, C.V. Thompson, Characterization of the young's modulus, residual stress and fracture strength of Cu-Sn-In thin films using combinatorial deposition and micro-cantilevers, J. Micromech. Microeng. 25 (3) (2015).
[22] B. Winiarski, M. Benedetti, V. Fontanari, M. Allahkarami, J.C. Hanan, P.J. Withers, High spatial resolution evaluation of residual stresses in shot peened specimens containing sharp and blunt notches by micro-hole drilling, micro-slot cutting and micro-X-ray diffraction methods, Exp. Mech. 56 (8) (2016) 1449–1463.
[23] M.D. Olson, M.R. Hill, A new mechanical method for biaxial residual stress mapping, Exp. Mech. 55 (6) (2015) 1139–1150.
[24] M.D. Olson, M.R. Hill, Two-dimensional mapping of in-plane residual stress with slitting, Exp. Mech. 58 (1) (2018) 151–166.
[25] E.G. Herbert, W.C. Oliver, M.P. de Boer, G.M. Pharr, Measuring the elastic modulus and residual stress of freestanding thin films using nanoindentation techniques, J. Mater. Res. 24 (9) (2011) 2974–2985.
[26] M. Ghidelli, M. Sebastiani, C. Collet, R. Guillemet, Determination of the elastic moduli and residual stresses of freestanding Au-TiW bilayer thin films by nanoindentation, Mater. Des. 106 (2016) 436–445.
[27] S. Suresh, A.E. Giannakopoulos, A new method for estimating residual stresses by instrumented sharp indentation, Acta Mater. 46 (16) (1998) 5755–5767.
[28] M. Sebastiani, C. Eberl, E. Bemporad, G.M. Pharr, Depth-resolved residual stress analysis of thin coatings by a new FIB-DIC method, Mater. Sci. Eng. A 528 (27) (2011) 7901–7908.
[29] E. Salvati, T. Sui, A.J.G. Lunt, A.M. Korsunsky, The effect of eigenstrain induced by ion beam damage on the apparent strain relief in FIB-DIC residual stress evaluation, Mater. Des. 92 (2016) 649–658.
[30] A.J.G. Lunt, N. Baimpas, E. Salvati, I.P. Dolbnya, T. Sui, S. Ying, H. Zhang, A.K. Kleppe, J. Dluhoš, A.M. Korsunsky, A state-of-the-art review of micron-scale spatially resolved residual stress analysis by FIB-DIC ring-core milling and other techniques, J. Strain Anal. Eng. Des. 50 (7) (2015) 426–444.
[31] J.W. Lim, H.S. Park, T.H. Park, J.J. Lee, J. Joo, Mechanical properties of titanium nitride coatings deposited by inductively coupled plasma assisted direct current magnetron sputtering, J. Vac. Sci. Technol. A 18 (2) (2000) 524–528.
[32] R. Daniel, E. Jager, J. Todt, B. Sartory, C. Mitterer, J. Keckes, Mono-textured nanocrystalline thin films with pronounced stress-gradients: on the role of grain boundaries in the stress evolution, J. Appl. Phys. 115 (20) (2014).
[33] M. Senn, Digital image correlation and tracking[Computer Software] https://uk.mathworks.com/matlabcentral/fileexchange/50994-digital-image-correlation-and-tracking 2015.

[34] A. Savitzky, M.J.E. Golay, Smoothing and differentiation of data by simplified least squares procedures, Anal. Chem. 36 (8) (1964) 1627–1639.

[35] G.S. Schajer, M.B. Prime, Use of inverse solutions for residual stress measurements, J. Eng. Mater. Technol. ASME 128 (3) (2006) 375–382.

[36] G.S. Schajer, Measurement of non-uniform residual stresses using the hole-drilling method. Part II—practical application of the integral method, J. Eng. Mater. Technol. 110 (4) (1988) 344–349.

[37] M. Barsanti, M. Beghini, L. Bertini, B.D. Monelli, C. Santus, First-order correction to counter the effect of eccentricity on the hole-drilling integral method with strain-gage rosettes, J. Strain Anal. Eng. Des. 51 (6) (2016) 431–443.

[38] A.M. Korsunsky, On the modelling of residual stresses due to surface peening using eigenstrain distributions, J. Strain Anal. Eng. Des. 40 (8) (2005) 817–824.

[39] A.T. DeWald, M.R. Hill, Eigenstrain-based model for prediction of laser peening residual stresses in arbitrary three-dimensional bodies part 2: model verification, J. Strain Anal. Eng. Des. 44 (1) (2009) 13–27.

[40] M. Achintha, D. Nowell, K. Shapiro, P.J. Withers, Eigenstrain modelling of residual stress generated by arrays of laser shock peening shots and determination of the complete stress field using limited strain measurements, Surf. Coat. Technol. 216 (2013) 68–77.

[41] M. Achintha, D. Nowell, Eigenstrain modelling of residual stresses generated by arrays of LSP shots, Procedia Eng. 10 (2011) 1327–1332.

[42] A.M. Korsunsky, J. Guénolé, E. Salvati, T. Sui, M. Mousavi, A. Prakash, E. Bitzek, Quantifying eigenstrain distributions induced by focused ion beam damage in silicon, Mater. Lett. 185 (2016) 47–49.

[43] T. Mura, Micromechanics of Defects in Solids, Springer, 1987.

[44] Y.-c. Wang, D.-g. Xie, X.-h. Ning, Z.-w. Shan, Thermal treatment-induced ductile-to-brittle transition of submicron-sized si pillars fabricated by focused ion beam, Appl. Phys. Lett. 106 (8) (2015) 081905.

[45] E. Salvati, L.R. Brandt, C. Papadaki, H. Zhang, S.M. Mousavi, D. Wermeille, A.M. Korsunsky, Nanoscale structural damage due to focused ion beam milling of silicon with Ga ions, Mater. Lett. 213 (2018) 346–349.

[46] J.M. Glasko, R.G. Elliman, J. Zou, D.J.H. Cockayne, J.D. Fitz Gerald, Strain and defect microstructure in ion-irradiated GeSi/Si strained layers as a function of annealing temperature, Appl. Phys. Lett. 73 (6) (1998) 838–840.

[47] A.J.G. Lunt, E. Salvati, L. Ma, I.P. Dolbnya, T.K. Neo, A.M. Korsunsky, Full in-plane strain tensor analysis using the microscale ring-core FIB milling and DIC approach, J. Mech. Phys. Solids 94 (2016) 47–67.

[48] E. Salvati, T. Sui, A.M. Korsunsky, Uncertainty quantification of residual stress evaluation by the FIB-DIC ring-core method due to elastic anisotropy effects, Int. J. Solids Struct. 87 (2016) 61–69.

[49] A.M. Korsunsky, M. Sebastiani, E. Bemporad, Focused ion beam ring drilling for residual stress evaluation, Mater. Lett. 63 (22) (2009) 1961–1963.

[50] A.J.G. Lunt, A.M. Korsunsky, A review of micro-scale focused ion beam milling and digital image correlation analysis for residual stress evaluation and error estimation, Surf. Coat. Technol. 283 (2015) 373–388.